

A High-Throughput Structural and Electrochemical Study of Metallic Glass Formation in Ni–Ti–Al

Howie Joress,* Brian L. DeCost, Suchismita Sarker, Trevor M. Braun, Sidra Jilani, Ryan Smith, Logan Ward, Kevin J. Laws, Apurva Mehta, and Jason R. Hattrick-Simpers



Cite This: *ACS Comb. Sci.* 2020, 22, 330–338



Read Online

ACCESS |



Metrics & More



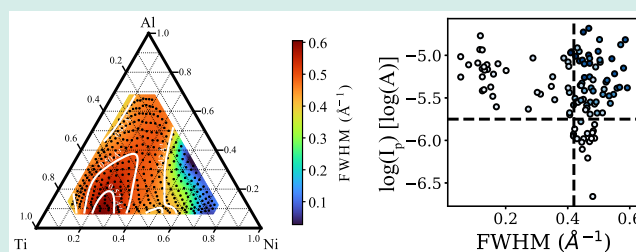
Article Recommendations



Supporting Information

ABSTRACT: On the basis of a set of machine learning predictions of glass formation in the Ni–Ti–Al system, we have undertaken a high-throughput experimental study of that system. We utilized rapid synthesis followed by high-throughput structural and electrochemical characterization. Using this dual-modality approach, we are able to better classify the amorphous portion of the library, which we found to be the portion with a full width at half maximum (fwhm) of $>0.42 \text{ \AA}^{-1}$ for the first sharp X-ray diffraction peak. Proper phase labeling is important for future machine learning efforts. We demonstrate that the fwhm and corrosion resistance are correlated but that, while chemistry still plays a role in corrosion resistance, a large fwhm, attributed to a glassy phase, is necessary for the highest corrosion resistance.

KEYWORDS: metallic glass, corrosion, high-throughput, machine learning, scanning droplet cell



INTRODUCTION

Metallic glasses are of great technological interest because they have been demonstrated to show superior properties, including high hardness and corrosion resistance, in comparison to their crystalline counterparts.^{1–3} To date, only around 6000 compositions have been explored and logged in tabulated formats.^{4,5} Therefore, there remain vast unexplored regions of composition space where metallic glasses with exciting properties may be found, as many as 3 million by some estimates.⁶ Unfortunately, it can be challenging to identify which alloys will have sufficient glass-forming ability (GFA). Due to the multiple length and time scales involved in solidification, accurate first-principles calculations of GFA have proven difficult.⁷ In lieu of these models, physiochemical based heuristic models have been developed. These include the well-known Turnbull model based on deep eutectics⁸ as well as more recent models including the efficient packing model⁹ and the model by Yang and Zhang¹⁰ based on atomic size variation and the ratio of the entropy to enthalpy of mixing. These models provide some guidance in searches for new metallic glasses, but as of yet they have not been demonstrated to be global predictors of alloys with a high GFA. Recently, we published a machine learning (ML) based model for the prediction of GFA that was iteratively coupled with high-throughput synthesis and characterization.⁵ This methodology demonstrated a significant increase in the rate of discovery (by a factor of 100–1000) of new metallic glass (MG) systems, and after several iterations, the predictions were determined to

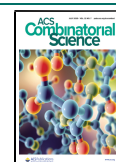
be reliable enough to pursue even when they violate the above heuristics.

However, high-throughput studies of MGs, including the one described above, are complicated due to the lack of methods for differentiating amorphous from crystalline samples.^{11–13} This is particularly true in thin films where calorimetric techniques are difficult.¹⁴ A common method in the literature, applied to both thin-film and bulk samples, is to measure the full width at half maximum (fwhm) of the first sharp diffraction peak (FSDP) in the X-ray diffraction from the sample. There is, however, no consensus on what values for this fwhm constitutes an MG. Further, it likely varies between systems. Many papers simply give a subjective description of the diffraction data, for instance stating that there are no sharp diffraction peaks.^{15–17} Ma et al.¹⁸ generalizes that MGs have an fwhm between 0.4 and fwhm between 0.4 \AA^{-1} and 0.5 \AA^{-1} ($\text{\AA} = 10^{-10} \text{ m}$). Reference 5 uses the fwhm for amorphous SiO_2 , 0.57 \AA^{-1} , as the threshold, a more conservative value than is typically applied in the literature. For ML model generation, frustratingly, much of the legacy data only catalogs the phase labeling and does not capture either the measured fwhm used to reach that classification or the raw X-ray diffraction data. As

Received: December 16, 2019

Revised: June 1, 2020

Published: June 4, 2020



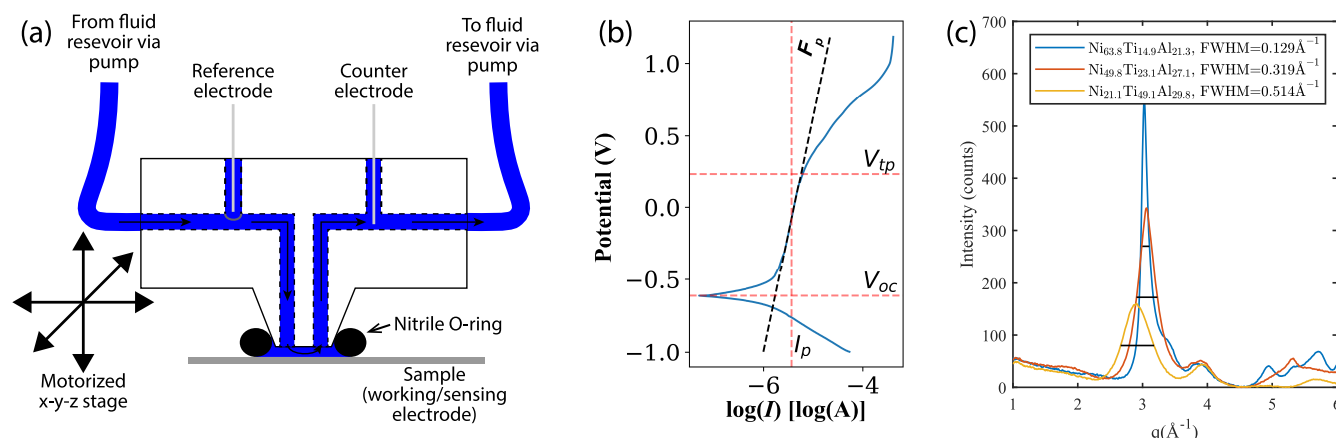


Figure 1. (a) Schematic showing the scan head of the SDC. The electrolyte flows through the scan head passing by the reference and counter electrodes as illustrated. The scan head is mounted on a motorized Z stage to enable contact of the scan head with the sample. The sample is mounted underneath the scan head on a motorized x-y stage to allow for rastering of the scan head over the sample. (b) A representative polarization curve showing extracted metrics: passivation current (I_p), open circuit potential (V_{oc}), flatness (F_p), and transpassive potential (V_{tp}). (c) Three examples of XRD curves from the sample with varying fwhm values of the FSDP. The fwhm is indicated for each pattern by a horizontal line.

a result, ML models, such as ours, built on this data, will similarly capture such variability in classification. In this work, we give an example of how applying a dual-modality screening approach can help sharpen the distinction between amorphous and crystalline alloys to improve future labeling.

In this paper, we explore an alloy system, Ni–Ti–Al. This system was selected for study because the regions of composition our machine learning model predicted to have a high GFA differed greatly between the predictions for bulk compared to thin-film alloys. We attribute this difference in part to different physics but also to the overlabeling of amorphous alloys in the literature as described above. Further, as will be reported below, the model predicted a large range of high GFA that extended far beyond the deep eutectic region located near the Ti_3Ni portion of the phase diagram.²⁰ The regions with high potential GFA included large swaths of the Ti–Al and Ni–Al binaries. This could be a technologically important material system as the presence of Al is likely to imbue the MG with the ability to resist corrosion in saline environments. For instance, this system could be of interest for coating Nitinol (Ni–Ti alloys) stents, where dissolution and absorption of nickel is potentially toxic and/or carcinogenic in nature.^{17,21} On the basis of these interesting ML predictions and applications, we proceeded with a traditional high-throughput study of this system.

Using combinatorial thin-film synthesis, we produced, in parallel, a range of alloys covering a large, central portion of the Ni–Ti–Al ternary system. We then rapidly characterized the resulting library with X-ray diffraction and electrochemical corrosion mapping. We found that there is a region of glass formation that extends beyond that which was previously demonstrated in the literature. We observe that the deepest glass-forming region, here determined by the region with the largest fwhm, was correlated with our bulk ML model, while relaxing the fwhm criteria resulted in a larger glass-forming region consistent with the thin-film ML model. Through the correlation of corrosion measurements with diffraction measurements, and consideration of the packing efficiency and electronic state of the alloys, we determined that a fwhm of 0.42 Å^{-1} for the FSDP is a good threshold for declaring a given

alloy amorphous in the Ni–Ti–Al system, a value much more conservative than that used in the literature for this system.

■ EXPERIMENTAL SECTION

A process flow diagram showing the various parts of the study, their interaction, and the use of ML is included in the Supporting Information (SI).

Machine Learning Model. This elemental system was selected on the basis of the ML model described in ref 5. In short, the model is a random forest model²² using the Magpie feature set as descriptors.²³ The probability of glass-forming ability (P_{GFA}) was predicted using the model as trained at the end of that work (including all the data published within, along with data from ref 4). Two types of predictions were made: The first uses only bulk MGs from the literature for predicting GFA in bulk alloys. The second is a stacked model, optimized for predicting GFA in thin films, trained using sputtered MG alloys with bulk model predictions as an input descriptor for each alloy.

Library Synthesis. Thin-film combinatorial libraries were synthesized by cosputtering a continuous composition spread from three elemental sources onto a 76 mm (3 in.) wafer. The geometry of the sputter guns was such that the centers of depositions for the three sources were off center from the wafer and the deposition rate for each source varied as a function of position across the wafer; thereby, a continuous composition spread is formed. In this case, we sputtered from metallic targets of Al, Ni, and Ti, each with purities of better than 99.99% with a power of 10.8 W/cm^2 , 1.07 W/cm^2 , and 4.28 W/cm^2 , respectively. Prior to sputtering, the base pressure of the chamber was better than $1.33 \times 10^{-4} \text{ Pa}$, and sputtering was done under a Ar (>99.99% purity) background of 0.67 Pa. Two nominally identical wafers were fabricated. The composition of the films was measured by scanning X-ray fluorescence (XRF) using a Bruker Tornado and analyzed by Crossroads XRS-MTFFP software.²⁴ The film was mapped with 177 points with an approximately 0.02 mm spot size.²⁵ Statistical error bars for concentration are $\pm 0.5\%$ for Ni and Ti and $\pm 2\%$ for Al, though larger systematic errors are possible, while unlikely. We interpolated these measurements across the wafer using a Gaussian process. After initial

characterization, one of the libraries was annealed at the base pressure of the chamber for 5 h at 400 °C with a ramp rate in both directions of 10 °C/min.

X-ray Characterization. The film was mapped using X-ray diffraction at the Stanford Synchrotron Radiation Light Source beamline 1-5.²⁶ Diffraction patterns for 362 points on the wafer were collected with 30 s of integration for each point. The details of the measurement and the code used to extract the full-width half-maximum (fwhm) of the first sharp diffraction peak (FSDP) are described in refs 5 and 27, and the source can be found at https://github.com/fang-ren/Discover_MG_CoVZr. A Gaussian process was fit to the fwhm values, as a function of composition, to allow for correlation with the electrochemical data. Examples of the data and fwhm are shown in Figure 1c.

Following annealing, the second sample was remeasured using a Bruker D8 diffracted using Cu K α radiation. The fwhm of the FSDP was captured by background subtracting the curve and then numerically calculating the fwhm.

Electrochemical Characterization. For electrochemical characterization, we used a scanning droplet cell (SDC), a millimeter/milliliter scale electrochemical cell optimized for localized electrochemical measurements similar to those described in refs 28–31. The SDC itself comprises a peristaltic pump, a fluid reservoir, and a scan head. The scan head, shown schematically in Figure 1, is a polytetrafluoroethylene block with a set of ports that can be sealed against the thin-film library with a nitrile O-ring. The pump pushes the electrolyte from the fluid reservoir, through the scan head into an isolated volume between the cell and the substrate, and back to the reservoir. As the fluid enters and exits this volume, it passes by a counter electrode (Pt wire) and reference electrode (Ag/AgCl in a saturated KCl solution), respectively. The metallic film comprising the sample acts as the working/sensing electrode. Corrosion measurements were performed by acquiring polarization curves in 1.1 mol/L NaCl (brine) solution pumped at 0.5 mL/min. To ensure the corrosion measurements were representative of the base metal, the bias was first swept negative from the open circuit potential to clean the surface, then swept positive to corrode the metal. Sweeping of the potential was done at a rate of 0.075 V/s, and the total scan range was –1 V to 1.2 V. Slightly different versions of the cell were used for the as-deposited and annealed films. For the measurements on the as-deposited film, the contact area for the electrolyte on the film is a circle with a 3.75 mm diameter and the measurements were taken on a 9 mm pitch checkerboard across the wafer. In total, we measured 109 points across the wafer, averaging 4.5 min of measurement time per point. For the annealed film, the probed area was increased to 7 mm, and 51 points were measured randomly on a 9 mm pitch grid.

The extracted features of interest from the polarization curves were the passivation current (I_p) and the flatness of the passivation plateau transpassive potential.³² The open circuit potential V_{oc} and transpassive potential (V_{tp}) were also tabulated and are provided in the SI. We obtain these features from each polarization curve by a stepwise fitting procedure, using the log absolute current as a function of potential, as illustrated in Figure 1b. The code can also be found in the SI. First, we fit a Laplace (i.e., a double exponential) peak model to the polarization curve to identify the open circuit potential V_{oc} (shown here just below –0.5 V). This model uses a fifth-order polynomial background to ensure the fit around the open

circuit potential is not biased by the shape of the rest of the polarization curve. We identify the onset of the passivation plateau as the potential corresponding to the 99th percentile of the Laplace peak model. Starting from this onset value, we fit a series of robust linear regression models to the rest of the polarization curve, constraining the model to pass through the onset point. We select the potential range for fitting these models by minimizing the mean squared error on the entire polarization curve. The passivation plateau flatness, F_p , is simply the slope of this linear model. Using this final robust linear model, we identify the transpassive potential V_{tp} by performing automatic threshold selection on the model residuals (using the triangle method³³). Finally, we report the passivation current I_p as the median log current of the passivation plateau. We note that the geometry of this electrochemical cell creates nonuniformities in flow leading to uneven corrosion of the wetted portion of the film. To this end, values should be taken as semiquantitative; relative values are informative for comparison, but the absolute values of the corrosion metrics have not been verified. It is also noted that a different scan head used between the two films limits absolute comparisons between the two sets of data.

RESULTS AND DISCUSSION

Machine Learning Models and Literature Data. Figure 2 shows the ML predictions of the Ni–Ti–Al system along with previous data from the literature. It is notable that a large portion of the alloys between those on the Ni–Ti binary and those with less than 20 at. % Al have not been explored in thin-films. Importantly, this region contains alloys that are closest in Ni/Ti ratio to the ideal shape memory alloy composition of Ni₃₀Ti₅₅Cu₁₅, found by Cui et al.³⁵ MGs in this range would likely be chemically compatible and exhibit limited Ni/Ti diffusion with ideal shape memory alloy stents.

The bulk model, shown in Figure 2a, predicted a limited region of glass formability, with only the Ni–Ti binary region showing a significant predicted GFA. This region is well correlated with the training data as well as the literature data from ref 34 and is located adjacent to the deep Ti₃Ni eutectic.²⁰ On the other hand, the stacked thin-film model, shown in Figure 2b, shows a much larger region of high predicted GFA, again well correlated with the training data with some interpolation between points. Interestingly, the atomic radii of Ti and Al are quite close to one another, and therefore, these alloys could be considered topologically as a binary system; therefore, there would ordinarily be little reason to expect such a large glass-forming region.

We attribute the larger predicted area to two factors. The first is that the physics of vapor deposition and bulk solidification are quite different, and it is well-known that sputtering is quite good at producing amorphous films. Beyond this, we believe the large predicted area has to do with the labeling in the training data. Despite the widths of XRD peaks being given as evidence for an amorphous structure, there is no precise structural definition of amorphous alloys, particularly on the basis of a measure of the fwhm of the FSDP. In our previous work, in the Co–Zr–X (X = V, Fe, and Ti), we used 0.57 Å^{–1}, on the basis of amorphous SiO₂, as the minimum fwhm of the FSDP for a glass. This value is very conservative, particularly in comparison to other published values. In this instance, for the Ni–Ti–Al system, there is a great variety of fwhm values that are given as evidence of an amorphous alloy. Using digital pixel-to-scale correlation, we were able to extract

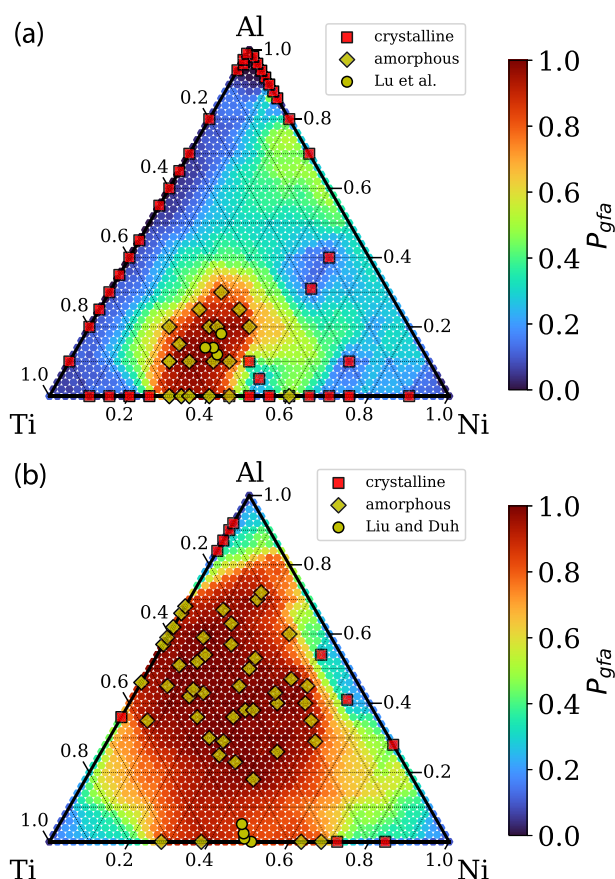


Figure 2. ML model predictions of MG formation for the Ni–Ti–Al system, displayed as a probability (P_{GFA}). (a) Bulk model and (b) stacked model for thin-films. Amorphous and crystalline data contained in the training set are plotted on the models along with the amorphous data points from refs 17 and 34 (not used in ML model).

the fwhm of the FSDP from XRD patterns published in the literature. Reference 34 correlates XRD with an $\approx 0.40 \text{ \AA}^{-1}$ fwhm of the FSDP with an amorphous phase for bulk alloys. Reference 17 uses an even narrower $\approx 0.33 \text{ \AA}^{-1}$ peak for classifying a thin-film alloy as glassy. Most importantly for our models, in ref 16, which forms the basis of our training set for thin films in this system, the minimum fwhm used to determine that a material was glassy was $\approx 0.28 \text{ \AA}^{-1}$ for $\text{Al}_{66}\text{Ti}_{34}$ (the largest fwhm for published XRD data in that work was $\approx 0.38 \text{ \AA}^{-1}$). It is likely this much softer boundary used for classifying thin films leads to the greater predictions of MG formation in thin-films as opposed to bulk. In a broader sense, it is this lack of specificity that makes modeling based on legacy data imprecise.

Observed Full Width at Half Maximum Values and Comparison to Literature. Figure 3a shows the fwhm of the FSDP, as measured by high-throughput X-ray diffraction from our as-deposited film as a function of composition. The sputtered film exhibits a fwhm that varies dramatically across the library from $\approx 0.1 \text{ \AA}^{-1}$ to $\approx 0.6 \text{ \AA}^{-1}$. The widest peak is seen in the region adjacent to the Ti_3Ni composition, predicted by our bulk model to be glass forming and previously reported in literature.^{17,34} Additionally, there is a valley in the fwhm extending from this region to Al_3Ni , a known intermetallic,³⁶ passing along the $\text{TiNi}_{0.5}\text{Al}_{1.5}$ intermetallic.³⁷ The general trend of the fwhm with composition is roughly consistent with the

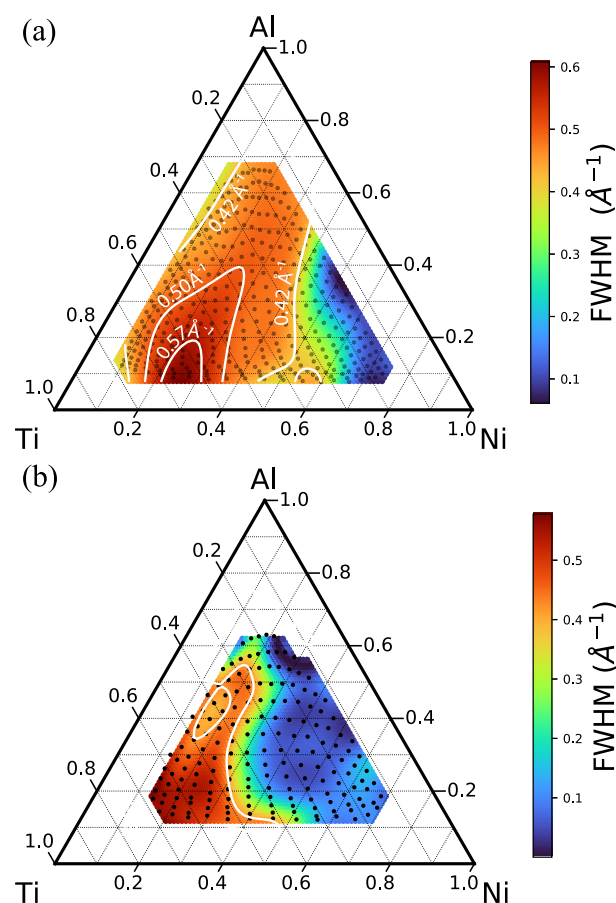


Figure 3. (a) Ternary plot showing the fwhm of the first bright diffraction peak as a function of composition for the as-deposited film. Interpolated values, using a Gaussian process, are plotted under points showing locations of XRD measurements. Isolines for fwhm corresponding to 0.57 \AA^{-1} , 0.5 \AA^{-1} , and 0.42 \AA^{-1} are included. (b) Similar plots for the fwhm of the FSDP for the annealed film. An isoline corresponding to 0.42 \AA^{-1} is included for reference.

work of Akiyama et al., where the inclusion of Al results in a sharpening of the FSDP. This observed extended range is similar to the thin-film predictions, with the exception that the fwhm narrows near the Ti–Al binary edge. We previously posited that, in sputtered MG films, glass formation was associated with the structural frustration associated with the quenched atoms being unable to order into their intermetallic structure, which is consistent with the observed variability in the fwhm.⁵

The portion of composition space that is amorphous given a range of fwhm cutoffs varies dramatically, as seen in Figure 3a. For the most conservative estimates of $\approx 0.57 \text{ \AA}^{-1}$ fwhm, only the region predicted by the bulk model can be considered to be amorphous. If, however, the criteria is systematically relaxed to be more consistent with the smaller literature values, then the range of observed glasses extends along the previously described valley and includes all measured alloys between 10 at. % and 50 at. % percent Ni. This is much more consistent with the thin-film model.

Figure 3b shows the fwhm for the annealed film. In this case, much more of the film has a narrow fwhm associated with crystalline phases. In particular, the Ni, and to a lesser extent, the Al rich alloys have small fwhm values while the Ti rich portion of the film maintains a large value. In both the as-

deposited and the annealed samples, there is a steep drop-off in fwhm below 0.42 \AA^{-1} . We attribute this to there being a boundary in the structure of the alloy between the crystalline and amorphous phases at this point. Above 0.42 \AA^{-1} the material is glassy, and therefore, the fwhm changes slowly. Below this point some or all of the alloy becomes crystalline. Since small crystallites are unstable, nano-crystals will only remain near the boundary, and therefore the fwhm falls sharply. This is even more apparent in the annealed sample, shown in Figure 3b, where the heat from the annealing accelerates grain growth.

Corrosion Mapping. Figure 4 shows two corrosion metrics extracted from the polarization curves measured

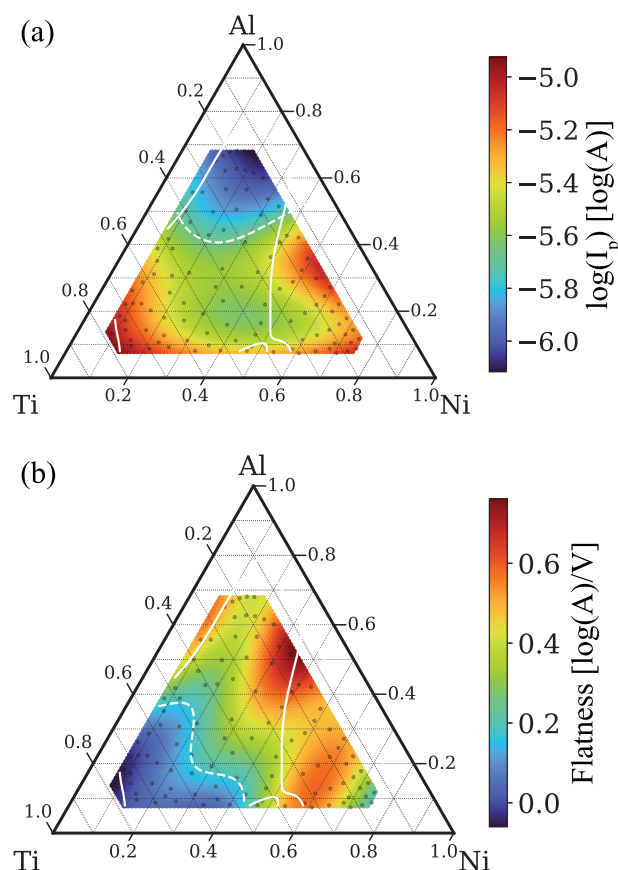


Figure 4. Results from the electrochemical measurements on the as-deposited sample. (a) The $\log(I_p)$ and (b) flatness. Measured data points are indicated by dots, and the data itself is interpolated with a Gaussian process. Both are annotated with the boundary of the glass region (solid white line) and optimal corrosion resistance (dotted white line).

using the scanning droplet cell on the as-deposited sample: passivation current (I_p) and flatness of the passivation plateau (F_p). (The other metrics, V_{tp} and V_{oc} , are included in the SI as they are not used in further analysis.)

The V_{oc} during the original anodic sweep is a measure of the mixed potential of the clean metal surface and the various reactants present in the electrolyte. As a function of composition, V_{oc} in this system largely follows a rule of mixtures; it is plotted in the SI. The general trend is that the Ni rich alloys are the most noble (less negative standard reduction potential), while Ti and Al alloys are more reactive. The I_p is taken to be the average of the log corrosion current in the

passivating regime and is an analogue for corrosion rate of the passivated surface. Here, the I_p shows good correlation with the fwhm; a clear valley in current density is visible in the range of alloys that exhibit the highest fwhm. In addition, the lowest values of I_p are observed in the regions with the highest Al concentration; this is sensible as Al is known to form passive films. The F_p of the plateau region is an estimate of the “stability” of the oxide scale growth rate to small perturbations during operation, with a small value being more stable. In this case, there is also good correlation between F_p and the fwhm. The chemistry of the alloy is important here as well, with the Ti rich samples exhibiting the lowest F_p , as illustrated in Figure 4b.

Akiyama et al. investigated the corrosion of Ni–Ti–Al alloys in 1 mol/L HCl, and it is illustrative to compare the compositional trends between their work and the present work. The I_p mapping is most comparable to corrosion rate (reported in mm/y). In the case of immersion in aerated HCl, increasing the Al content resulted in an order of magnitude increase in the corrosion rate from 0.1 mm/year to 2.0 mm/year. The corrosion rate was relatively insensitive to the ratio of Ni to Ti, although from the published diffraction data, it was correlated to the diffraction fwhm. Conversely, in our case, using 1 mol/L NaCl, we see that Al additions are responsible for an order of magnitude decrease in the corrosion current and the alloys containing the most Ti and Ni (and also the largest fwhm) corrode the quickest. For an alloy to be corrosion resistant, it must be thermodynamically stable (i.e., the metal itself must be stable or it must form an oxide, hydroxide, etc. instead of actively dissolving into ions) and any oxide/hydroxide scale must have slow growth kinetics. For instance, from the Pourbaix diagram, in 1 mol/L HCl Al, Ni and their oxides/hydroxides actively dissolve (corrode) for all but the most cathodic potentials.^{38–40} Conversely, Ti forms a stable oxide phase with slow growth kinetics for the entire potential voltage range of water stability. Near neutral pH Al and Ti form stable oxides, and thus, the corrosion rate is determined by the growth rate of the oxides or hydroxides formed. According to the theoretical Pourbaix diagrams, Ni alone may actively dissolve at neutral pH (depending on Ni ion concentration), although experimental observations are that the corrosion rate is slow.⁴¹ That being said, based on Materials Project models, Ni alloys containing Al or Ti will generally form TiO_2 or Al_2O_3 oxides on their surfaces at neutral pH.⁴² In practice, mixed metal oxides can be expected to form whose corrosion rates will vary significantly from the pure metal oxides contained within the Materials Project database.

Correlating Corrosion with Glass Formation. It is known that metallic glasses in many cases exhibit better resistance to corrosion than their crystalline counterparts.^{3,43} There are a variety of reasons for this. In MGs, high-energy crystalline defects (e.g., grain boundaries, lattice vacancies, dislocations) are unavailable, and therefore, localized pitting corrosion is inhibited. Perhaps more importantly in this case, MGs are known to more readily form passivating oxides. Finally, due to the lack of an ordered lattice, ionic conduction through the material is retarded, slowing corrosion. This potential for enhanced corrosion resistance provides a second method of evaluating the glassy nature of our films.

Figure 5 plots the I_p and F_p as a function of fwhm and Ti concentration in the alloy (as color) for the Ni–Ti–Al samples. It is clear in both of these plots that there is a fwhm

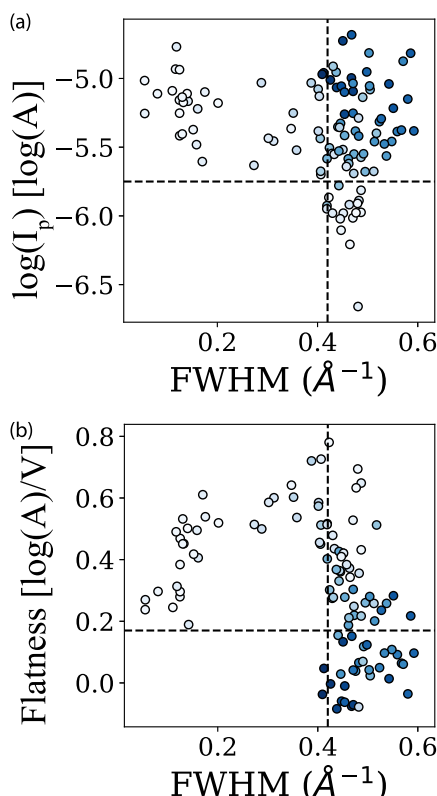


Figure 5. Plots of $\log(I_p)$ and F_p as a function of fwhm of the FSDP. It can be seen that, in both cases, the lowest values only exist at a high fwhm. For alloys to have, in panel a, $\log(I_p) < -5.75$, and in panel b, $F_p < 0.17$ requires a fwhm value $> 0.42 \text{ \AA}^{-1}$. The blue color scale is used to indicate Ti content with darker colors indicating a greater concentration of Ti.

threshold above which the lowest currents and flatness are observed. Specifically, for I_p we can create a threshold in fwhm at 0.42 \AA^{-1} and in $\log(I_p)$ at -5.75 . Any corrosion current below $\log(I_p) = -5.75$ must have a fwhm above 0.42 \AA^{-1} . These points can be as much as half an order of magnitude lower than any of the data below the fwhm threshold. Further, there is a clear relationship between the Ti concentration and the corrosion current beyond that threshold. The samples with

the lowest Ti concentration (or greatest Al concentration) show the lowest corrosion rates.⁴⁴ According to the published Pourbaix diagrams, Al and Ti should form passive oxides at neutral pH in the presence of Cl^- ions for the potential range of interest.^{39,40,45} Conversely, Ni in similar environments, depending on ion concentration, can either be corroding or passivating, though experimentally it is known to passivate. Therefore, in this context, the relative corrosion rates will primarily be determined by the protective nature of the passivating oxide or hydroxide. Similar trends in increased corrosion resistance by the addition of Al have been observed in TiN coatings.⁴⁶

A similar classification behavior is observed in the F_p vs fwhm plots, whereby a fwhm of 0.42 \AA^{-1} is a necessary, but not sufficient, condition, to have a flatness below $0.17 \log(A)/V$. Here, the opposite compositional variation with Ti and Al concentrations is observed. In this case, the larger Ti concentrations are positively correlated with the smallest flatness values. In this alloy system, there appears to be a trade-off between the corrosion rate (Al concentration) and stability of the oxide to external perturbation (Ti concentration). From the observation of the corrosion properties of the Ni–Ti–Al alloys, and the previous values provided in the literature, it appears that for this system a fwhm value of 0.42 \AA^{-1} is more reasonable for declaring the deposited films as being amorphous. It is interesting to note that a similar trend in corrosion rate and fwhm is observed by Akiyama et al.

To separate the effect of structure from chemistry, we annealed a nominally identical wafer under vacuum for 5 h at 400°C so that a large portion of the wafer was crystallized, particularly in the Al and Ni rich portions of the wafer. We then performed electrochemical measurements on the wafer as above. Figure 6a,b plots the two clusters of probed points on either side of the crystalline amorphous boundary. Figure 6a shows the polarization curve for three compositionally similar points with $\sim 45\%$ Al: one glassy with a fwhm of the FSDP of 0.45 \AA^{-1} and two crystalline with FWHM values of 0.34 \AA^{-1} and 0.31 \AA^{-1} , respectively. We can see that the two crystalline regions have a higher corrosion rate and lower passivation than the glassy region over the measured ranges. This is true even for the second crystalline point which has a lower Ni content and therefore should be expected to have a higher corrosion

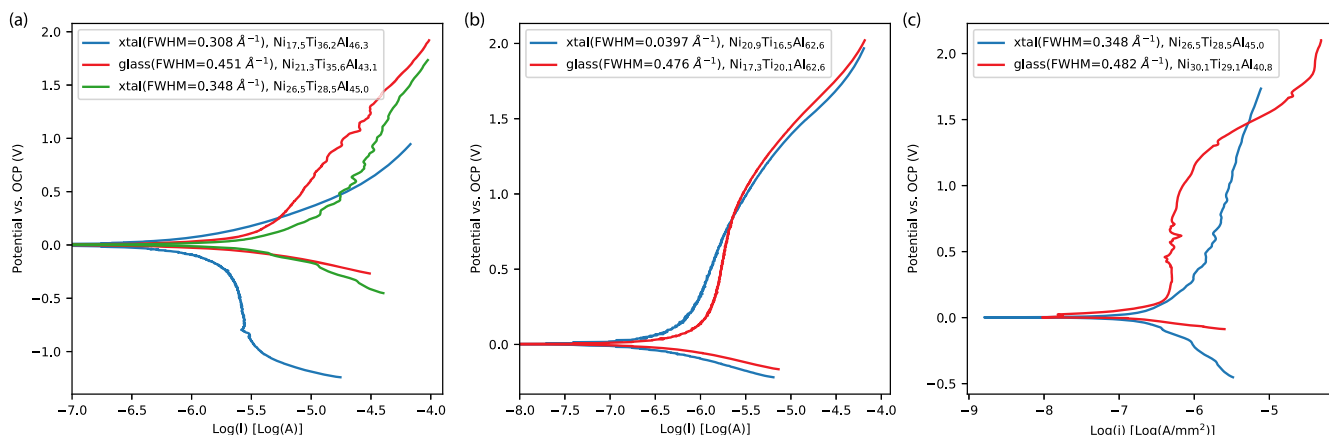


Figure 6. (a) Comparison of the polarization curves for three alloys with similar compositions including $\sim 45\%$ Al in both the glassy and crystalline (xtal) regions of the annealed sample. (b) Comparison between a pair of alloys on the annealed film of similar composition including $\sim 62\%$ Al. (c) Pair of alloys, one from the annealed film (crystalline) and one from the as-deposited film (glass). In this case we have normalized the current by alloy area to a current density, j . Additional comparisons are shown in the SI.

rate. Importantly, these measurements were made on alloys that are in the region contributing to the low passivation current in Figure 5a. The other cluster of points is much higher in Al content, ~62% Al, shown in Figure 6b. In this case, the curves are very similar, with the glass region showing slightly higher corrosion current. We can attribute this lack of effect of structure on the corrosion to two things. First, there may be enough Al in the alloy that the passivation is sufficiently strong without a structural effect (the corrosion current is much lower than the previous example). Second, the higher corrosion current in the crystalline phase in the previous example may be an effect of not just ordered structure, but of nanoscale crystallites, associated with broad diffraction peaks, that are known to have higher corrosion rates.⁴⁷ The crystalline sample in the Al rich case has much coarser grains and therefore will similarly have a better corrosion resistance. Both effects still provide a route for gleaming structural information from the corrosion measurements.

To further separate the effect of chemistry and structure on the corrosion trends, we can compare data from the as-deposited and annealed samples. While we have accounted for a change in the contact area, absolute comparisons are still complicated by the differing measurement geometries. However, it is possible to observe the trends in the polarization curves themselves. For each data point measured on the annealed film, we found the nearest point in composition space measured on the as-deposited film. Figure 6c shows a comparison of one of the crystalline points from Figure 6a ($\text{fwhm} = 0.34 \text{ \AA}^{-1}$) with a similar composition on the as-deposited sample that we identify as a glassy phase. Again, as expected, the glassy material has a much flatter passivation plateau and most likely lower I_p . Polarization curves from other samples are shown in the SI with many having similar trends.

Efficient Packing and Electronic Stability. Laws et al.⁹ provides a model for glass stability based on the ability of a given alloy to form efficiently packed clusters. Figure 7 plots the fwhm surface along with lines demarcating the efficiently packed clusters and isoelectronic configurations, and the

liquidus projection. As mentioned above, Ti_2Ni liquidus phase field is highly depressed in temperature and indicates that this phase might be difficult to crystallize. The fwhm valley corresponds to a series of phase boundaries and temperature troughs running through the Ti and Al rich segments of the liquidus surface. This is likely to be associated with topological or electronic stability. Calculations using the atomic packing efficiency model (ref 9) were made assuming atomic radii of 125 pm, 142 pm, and 144 pm for Ni, Al, and Ti. These calculations show there is nearly an overlap of compositions that are capable of forming efficiently packed Ni-centered (icosahedral-like) clusters with a coordination number of $\langle 12 \rangle$ with Al/Ti-centered efficiently packed clusters with a coordination number of $\langle 14 \rangle$. According to the atomic packing efficiency model, compositions that are capable of forming these clusters are likely to have high GFA. Given this model, it is unsurprising that there is a distinct correlation between the packing efficiency line, the liquidus lines, and the fwhm valley. Further, the valence electrons per cluster, with Ni = 0, Ti = 2, and Al = 3, show a very good correlation between e^-/c (electrons per cluster) = 18 and $e^-/c = 20$ lines and the fwhm. Note that the liquidus lines bounding the Ti_2Ni phase field follow the two e/c lines. The largest fwhm values reside in the regions that satisfy both the efficient packing and the electrons per cluster models. The fwhm valley follows both the liquidus line and the efficient packing model, possibly indicating a weaker glass-forming ability as Al is substituted for Ti.

SUMMARY

We have performed high-throughput synthesis and structural and electrochemical screening of an MG Ni–Ti–Al thin-film library. We show that there is a correlation between the fwhm of the FSDP and the highest corrosion resistance. We used this correlation to determine that 0.42 \AA^{-1} is a reasonable threshold for fwhm of the FSDP in this system for classifying a material as an MG. Using this threshold and the fwhm map, we further show that the area we consider to be glassy is much larger than the bulk ML model suggests, but it generally agrees well with both our stacked ML model as well as the efficient packing model. While this particular threshold is specific to this system, we believe that this method of using correlation between two screening modalities can be useful in other classification problems based on continuously varying measured quantities. Our selection of a different criteria for MG classification leads to interesting questions about the model: How well classified is the cataloged data used to train the ML model? How much does a change in classification criteria for new high-throughput data affect new predictions? Most importantly and most generally, how do we handle usage of literature and cataloged data, such as ref 4, that do not have the necessary detail to allow for a consistent application of a classification criteria?

A series of bulk samples have been fabricated on the basis of the results from the ML-HTE work described here using vacuum casting. The molten droplets exhibited a high-wetting angle and slow solidification kinetics, attributes often associated with glass-forming melts. Bulk metallic glass formation has been confirmed for alloys in the range $\text{Ti}_{52.5-62.5}\text{Ni}_{30-35}\text{Al}_{7.5-15}$ of up to 2 mm critical casting diameter. This work is forthcoming and will be published elsewhere shortly.

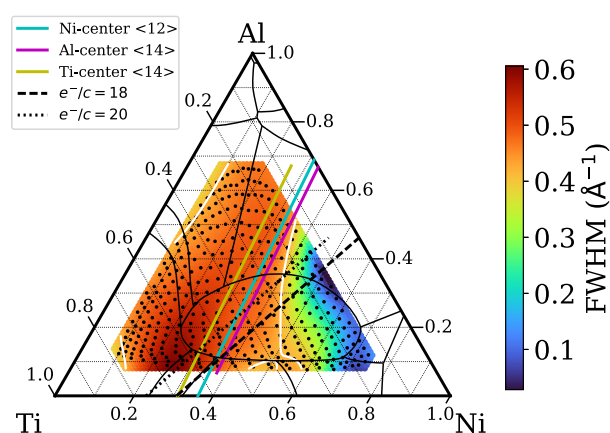


Figure 7. Plot of compositions with efficiently packed clusters and iso-electronic stability based on the model by Laws et al.⁹ The close packed lines drawn include a Ni-centered cluster with 12 atom coordination, Al-centered cluster with 14 atom coordination, and a Ti-centered cluster with 14 atom coordination. Isoelectronic lines are drawn showing the number of valence electrons per cluster for the Ni-centered clusters, assuming valence electrons per atom of Ni = 0, Ti = 2, and Al = 3. The liquidus phase lines from ref 20 have also been superimposed onto the phase diagram.

■ ASSOCIATED CONTENT

Supporting Information

The Supporting Information is available free of charge at <https://pubs.acs.org/doi/10.1021/acscombsci.9b00215>.

Additional figures including V_{oc} and V_{tp} , and a comparison of polarization curves (PDF)

■ AUTHOR INFORMATION

Corresponding Author

Howie Joress — Materials Measurement Science Division, National Institute of Standards and Technology, Gaithersburg, Maryland 20899, United States; orcid.org/0000-0002-6552-2972; Email: howie.joress@nist.gov

Authors

Brian L. DeCost — Materials Measurement Science Division, National Institute of Standards and Technology, Gaithersburg, Maryland 20899, United States

Suchismita Sarker — Stanford Synchrotron Radiation Lightsource, SLAC National Accelerator Laboratory, Menlo Park, California 94025, United States; orcid.org/0000-0002-8820-1143

Trevor M. Braun — Materials Science and Engineering Division, National Institute of Standards and Technology, Gaithersburg, Maryland 20899, United States

Sidra Jilani — School of Materials Science and Engineering, University of New South Wales, Sydney, New South Wales 2052, Australia

Ryan Smith — Materials Measurement Science Division, National Institute of Standards and Technology, Gaithersburg, Maryland 20899, United States

Logan Ward — Department of Materials and Engineering, Northwestern University, Evanston, Illinois 60208, United States; orcid.org/0000-0002-1323-5939

Kevin J. Laws — School of Materials Science and Engineering, University of New South Wales, Sydney, New South Wales 2052, Australia

Apurva Mehta — Stanford Synchrotron Radiation Lightsource, SLAC National Accelerator Laboratory, Menlo Park, California 94025, United States; orcid.org/0000-0003-0870-6932

Jason R. Hatrick-Simpers — Materials Measurement Science Division, National Institute of Standards and Technology, Gaithersburg, Maryland 20899, United States

Complete contact information is available at:

<https://pubs.acs.org/doi/10.1021/acscombsci.9b00215>

Notes

The authors declare no competing financial interest.

Data and code used in this work including 1D diffraction data, polarization curves, extracted metrics, and data analysis and plotting code can be found here: <https://github.com/usnistgov/HTE-NiTiAl> (DOI 10.5281/zenodo.3871786).

■ ACKNOWLEDGMENTS

The authors thank Doug van Campen for assistance with collecting the XRD, which was collected at the Stanford Synchrotron Radiation Light-Source, SLAC National Accelerator Laboratory, which is supported by the U.S. Department of Energy, Office of Science, Office of Basic Energy Sciences under Contract DE-AC02-76SF00515. H.J. and B.L.D. thank the NIST/NRC postdoctoral fellows program for support. S.S. was supported by the Advanced Manufacturing Office of the

Department of Energy under grant FWP-100250. The ML work and L.W. were funded under Award 70NANB19H005 from U.S. Department of Commerce, National Institute of Standards and Technology, as part of the Center for Hierarchical Materials Design (CHiMaD).

■ REFERENCES

- (1) Ashby, M.; Greer, A. Metallic glasses as structural materials. *Scr. Mater.* **2006**, *54*, 321–326.
- (2) Khan, M. M.; Nemati, A.; Rahman, Z. U.; Shah, U. H.; Asgar, H.; Haider, W. Recent Advancements in Bulk Metallic Glasses and Their Applications: A Review. *Crit. Rev. Solid State Mater. Sci.* **2018**, *43*, 233–268.
- (3) Scully, J. R.; Gebert, A.; Payer, J. H. Corrosion and related mechanical properties of bulk metallic glasses. *J. Mater. Res.* **2006**, *22*, 302–313.
- (4) Kawazoe, Y. Nonequilibrium Phase Diagrams of Ternary Amorphous Alloys. *LB: New Ser., Group III: Condensed* **1997**, *37*, 1–295.
- (5) Ren, F.; Ward, L.; Williams, T.; Laws, K. J.; Wolverton, C.; Hatrick-Simpers, J.; Mehta, A. Accelerated discovery of metallic glasses through iteration of machine learning and high-throughput experiments. *Science advances* **2018**, *4*, No. eaaq1566.
- (6) Li, Y.; Zhao, S.; Liu, Y.; Gong, P.; Schroers, J. How many bulk metallic glasses are there? *ACS Comb. Sci.* **2017**, *19*, 687–693.
- (7) Perim, E.; Lee, D.; Liu, Y.; Toher, C.; Gong, P.; Li, Y.; Simmons, W. N.; Levy, O.; Vlassak, J. J.; Schroers, J.; Curtarolo, S. Spectral descriptors for bulk metallic glasses based on the thermodynamics of competing crystalline phases. *Nat. Commun.* **2016**, *7*, 12315.
- (8) Marcus, M.; Turnbull, D. On the correlation between glass-forming tendency and liquidus temperature in metallic alloys. *Mater. Sci. Eng.* **1976**, *23*, 211–214.
- (9) Laws, K.; Miracle, D.; Ferry, M. A predictive structural model for bulk metallic glasses. *Nat. Commun.* **2015**, *6*, 8123.
- (10) Yang, X.; Zhang, Y. Prediction of high-entropy stabilized solid-solution in multi-component alloys. *Mater. Chem. Phys.* **2012**, *132*, 233–238.
- (11) Schnabel, V.; Köhler, M.; Evertz, S.; Gamcova, J.; Bednarcik, J.; Music, D.; Raabe, D.; Schneider, J. M. Revealing the relationships between chemistry, topology and stiffness of ultrastrong Co-based metallic glass thin films: A combinatorial approach. *Acta Mater.* **2016**, *107*, 213–219.
- (12) Javed, A.; Khan, M. M.; Camiller, J.; Greenlee-Wacker, M.; Haider, W.; Shabib, I. Property optimization of Zr-Ti-X (X = Ag, Al) metallic glass via combinatorial development aimed at prospective biomedical application. *Surf. Coat. Technol.* **2019**, *372*, 278–287.
- (13) Hui, J.; Ma, H.; Wu, Z.; Zhang, Z.; Ren, Y.; Zhang, H.; Zhang, L.; Wang, H. High-throughput investigation of crystal-to-glass transformation of Ti–Ni–Cu ternary alloy. *Sci. Rep.* **2019**, *9*, 19932.
- (14) McCluskey, P. J.; Vlassak, J. J. Glass transition and crystallization of amorphous Ni–Ti–Zr thin films by combinatorial nano-calorimetry. *Scr. Mater.* **2011**, *64*, 264–267.
- (15) Ding, S.; Liu, Y.; Li, Y.; Liu, Z.; Sohn, S.; Walker, F. J.; Schroers, J. Combinatorial development of bulk metallic glasses. *Nat. Mater.* **2014**, *13*, 494–500.
- (16) Akiyama, E.; Habazaki, H.; Kawashima, A.; Asami, K.; Hashimoto, K. In *Proceedings of the Symposium on Corrosion, Electrochemistry, and Catalysis of Metastable Metals and Intermetallics*; Clayton, C. R., Hashimoto, K., Eds.; Electrochemical Society, 1993; Vol. 93–30, pp 26–37.
- (17) Liu, K.; Duh, J. Effect of aluminum on the corrosion behavior of NiTiAl thin films. *Appl. Surf. Sci.* **2007**, *253*, S268–S273.
- (18) Ma, D.; Stoica, A. D.; Wang, X.-L. Power-law scaling and fractal nature of medium-range order in metallic glasses. *Nat. Mater.* **2009**, *8*, 30.
- (19) $\text{\AA} = 10^{-10} \text{ m}$.
- (20) Budberg, P. *Ternary Alloys*; Verlag Chemie Weinheim, 1992; Vol. 7; pp 7–20.

- (21) Thierry, B.; Tabrizian, M.; Trepanier, C.; Savadogo, O.; Yahia, L. Effect of surface treatment and sterilization processes on the corrosion behavior of NiTi shape memory alloy. *J. Biomed. Mater. Res.* **2000**, *51*, 685–693.
- (22) Breiman, L. Random forests. *Machine learning* **2001**, *45*, 5–32.
- (23) Ward, L.; Agrawal, A.; Choudhary, A.; Wolverton, C. A general-purpose machine learning framework for predicting properties of inorganic materials. *npj Computational Materials* **2016**, *2*, 16028.
- (24) Certain commercial equipment, instruments, software, or materials are identified in this paper to foster understanding. Such identification does not imply recommendation or endorsement by the National Institute of Standards and Technology, nor does it imply that the materials or equipment identified are necessarily the best available for the purpose.
- (25) Hattrick-Simpers, J. R.; Zakutayev, A.; Barron, S. C.; Trautt, Z. T.; Nguyen, N.; Choudhary, K.; DeCost, B.; Phillips, C.; Kusne, A. G.; Yi, F.; Mehta, A.; Takeuchi, I.; Perkins, J. D.; Green, M. L. An Inter-Laboratory Study of Zn–Sn–Ti–O Thin Films using High-Throughput Experimental Methods. *ACS Comb. Sci.* **2019**, *21*, 350–361.
- (26) Gregoire, J.; Van Campen, D.; Miller, C.; Jones, R.; Suram, S.; Mehta, A. High-throughput synchrotron X-ray diffraction for combinatorial phase mapping. *J. Synchrotron Radiat.* **2014**, *21*, 1262–1268.
- (27) Ren, F.; Pandolfi, R.; Van Campen, D.; Hexemer, A.; Mehta, A. On-the-fly data assessment for high-throughput X-ray diffraction measurements. *ACS Comb. Sci.* **2017**, *19*, 377–385.
- (28) Woodhouse, M.; Parkinson, B. Combinatorial approaches for the identification and optimization of oxide semiconductors for efficient solar photoelectrolysis. *Chem. Soc. Rev.* **2009**, *38*, 197–210.
- (29) Klemm, S. O.; Schauer, J.-C.; Schuhmacher, B.; Hassel, A. W. High throughput electrochemical screening and dissolution monitoring of Mg–Zn material libraries. *Electrochim. Acta* **2011**, *56*, 9627–9636.
- (30) Klemm, S. O.; Kollender, J. P.; Hassel, A. W. Combinatorial corrosion study of the passivation of aluminium copper alloys. *Corros. Sci.* **2011**, *53*, 1–6.
- (31) Gregoire, J. M.; Xiang, C.; Liu, X.; Marcin, M.; Jin, J. Scanning droplet cell for high throughput electrochemical and photo-electrochemical measurements. *Rev. Sci. Instrum.* **2013**, *84*, 024102.
- (32) Jones, D. A. *Principles and Prevention of Corrosion*; Macmillan, 1992.
- (33) Zack, G. W.; Rogers, W. E.; Latt, S. Automatic measurement of sister chromatid exchange frequency. *J. Histochem. Cytochem.* **1977**, *25*, 741–753.
- (34) Lu, B.-c.; Li, Y.; Xu, J. Optimal glass-forming composition and its correlation with eutectic reaction in the Ti–Ni–Al ternary system. *J. Alloys Compd.* **2009**, *467*, 261–267.
- (35) Cui, J.; Chu, Y. S.; Famodu, O. O.; Furuya, Y.; Hattrick-Simpers, J.; James, R. D.; Ludwig, A.; Thienhaus, S.; Wuttig, M.; Zhang, Z.; Takeuchi, I. Combinatorial search of thermoelastic shape-memory alloys with extremely small hysteresis width. *Nat. Mater.* **2006**, *5*, 286.
- (36) Nash, P.; Singleton, M.; Murray, J. Al–Ni (Aluminum–Nickel). *Phase Diagrams of Binary Nickel Alloys*; ASM International, 1991; Vol. 1, pp 3–11.
- (37) Zeng, K.; Schmid-Fetzer, R.; Huneau, B.; Rogl, P.; Bauer, J. The ternary system Al–Ni–Ti part II: thermodynamic assessment and experimental investigation of polythermal phase equilibria. *Intermetallics* **1999**, *7*, 1347–1359.
- (38) Alfantazi, A.; Ahmed, T.; Tromans, D. Corrosion behavior of copper alloys in chloride media. *Mater. Eng.* **2009**, *30*, 2425–2430.
- (39) Davoodi, A.; Pan, J.; Leygraf, C.; Norgren, S. Multianalytical and in situ studies of localized corrosion of EN AW-3003 alloy-influence of intermetallic particles. *J. Electrochem. Soc.* **2008**, *155*, C138–C146.
- (40) Bhola, R.; Bhola, S. M.; Mishra, B.; Olson, D. L. Electrochemical behavior of titanium and its alloys as dental implants in normal saline. *Advances in Physical Chemistry* **2009**, *2009*, 574359.
- (41) Deltombe, E.; de Zoubov, N.; Pourbaix, M. *Atlas of Electrochemical Equilibria in Aqueous Solutions*, 2nd ed.; NACE, 1974; pp 330–342.
- (42) Persson, K. A.; Waldwick, B.; Lazic, P.; Ceder, G. Prediction of solid-aqueous equilibria: Scheme to combine first-principles calculations of solids with experimental aqueous states. *Phys. Rev. B: Condens. Matter Mater. Phys.* **2012**, *85*, 235438.
- (43) Waseda, Y.; Aust, K. Corrosion behaviour of metallic glasses. *J. Mater. Sci.* **1981**, *16*, 2337–2359.
- (44) Thomas, R. Titanium in the geothermal industry. *Geothermics* **2003**, *32*, 679–687.
- (45) Skilbred, E. S. Corrosion of Nickel-Aluminium Bronze—How Does the Different Alloying Elements Effect the Corrosion Properties?. M.Sc. Thesis, NTNU, 2016.
- (46) Li, Y.; Qu, L.; Wang, F. The electrochemical corrosion behavior of TiN and (Ti, Al) N coatings in acid and salt solution. *Corros. Sci.* **2003**, *45*, 1367–1381.
- (47) Mishra, R.; Balasubramaniam, R. Effect of nanocrystalline grain size on the electrochemical and corrosion behavior of nickel. *Corros. Sci.* **2004**, *46*, 3019–3029.